

Zwischenbericht 2015

Förderprogramm:	Virtuelle Institute
Impulsfonds-Projektnummer:	VH-VI-403
Projekttitel:	In-Situ Nano-Imaging of Biological and Chemical Processes
Federführende/r Wissenschaftler/in	Christian Schroer
Berichtszeitraum (Förderungszeitraum)	01.01.2015 – 31.12.2015

Sachbericht**1 Fortschritt des im Antrag beschriebenen Arbeitsprogramms**

In the framework of this VI, the following sub-projects have been addressed during the year 2015:

- 1.1 Phase contrast tomography of mouse lung: from whole animal to tissue and to the sub-cellular level (AG Salditt)
- 1.2 Development of microfluidic platforms to study biological matter by x-rays (AG Köster)
- 1.3 Combined ptychography and nano-diffraction for cellular imaging (AG Köster & AG Schroer)
- 1.4 X-ray nanoprobe analysis of diatoms (AG Rosenhahn)
- 1.5 Biological samples: small angle x-ray scattering resolves internal composition of *E. coli* cells (AG Rosenhahn)
- 1.6 Design of in-situ cell for ptychography and time-resolved imaging of catalyst aging during the sintering process (AG Grunwaldt & AG Schroer)
- 1.7 Application of the new lithographically etched silicon in-situ reactor for 2D study of catalytic reactions: x-ray imaging and spectroscopic studies (AG Grunwaldt)
- 1.8 Towards 3D imaging of heterogeneous catalysts: structural changes and reaction gradients observed by in situ tomography (AG Grunwaldt)
- 1.9 Microfluidic reactor for studies on early stage kinetics and formation of metallic nanoparticles, colloids and precipitates (AG Grunwaldt)
- 1.10 Morphological analysis of ceriumoxide stabilized nanoporous gold catalysts with resonant soft x-ray scattering (AG Rosenhahn & AG Grunwaldt)

- 1.11 In-situ x-ray diffraction studies of structural evolution of colloidal crystal films formed by polystyrene spherical particles upon heating (AG Vartanyants)
- 1.12 Soft x-ray ptychographic imaging of diatoms (AG Vartanyants & AG Rosenhahn)
- 1.13 Strain mapping in core-shell nanowires by coherent x-ray diffraction imaging (AG Vartanyants & AG Schroer)
- 1.14 Implementation of a total fluorescence yield NEXAFS mode for HORST (AG Rosenhahn)
- 1.15 X-ray microscope at beamline P11 (AG Meents)

These sub-projects are described in more detail below.

1.1 Phase contrast tomography of mouse lung: from whole animal to tissue and to the sub-cellular level (AG Salditt)

Tomography of biological tissues under physiological conditions has been a major focus within this VI. We have used propagation-based hard x-ray phase-contrast tomography of mouse lung-tissue covering multiple length scales from the whole animal down to the sub-cellular level with nanoscale resolution. With a liquid-metal jet source, studies on whole mice can be performed under in-situ conditions [27]. By utilizing optimized phase retrieval algorithms, quantitative reconstructions can be obtained that enable automatic renderings without edge artifacts at 5 μm resolution. To extend the method to nanoscale resolution we use x-ray waveguides at synchrotron radiation facilities, which provide the necessary well-controlled cone-beam illumination, which allows propagation imaging at highest magnification and resolution [1]. Due to the small Fresnel numbers in this geometry the measured images are of holographic nature, which raises the need for sophisticated phase retrieval. While the waveguides allow 2D imaging at 23 nm resolution [1], the achievable 3D resolution may be lower due to practical reasons like sample drift or vibrations. Using local tomography in large samples, we demonstrate reconstructions of in-situ lung tissue with a resolution down to 160 nm [2] and down to 50 nm on thick-samples-contained fixed cells (cf. Fig. 1). To achieve the latter, we impose consistency of the dataset for automatic alignment and we develop new algorithms that impose less constraints and use an overlap constraint of different tomographic projections for a combined 3D phase retrieval [28].

We have completed the project (Mem3b) with the publication of [3]. Fig. 2 illustrates the result of the work.

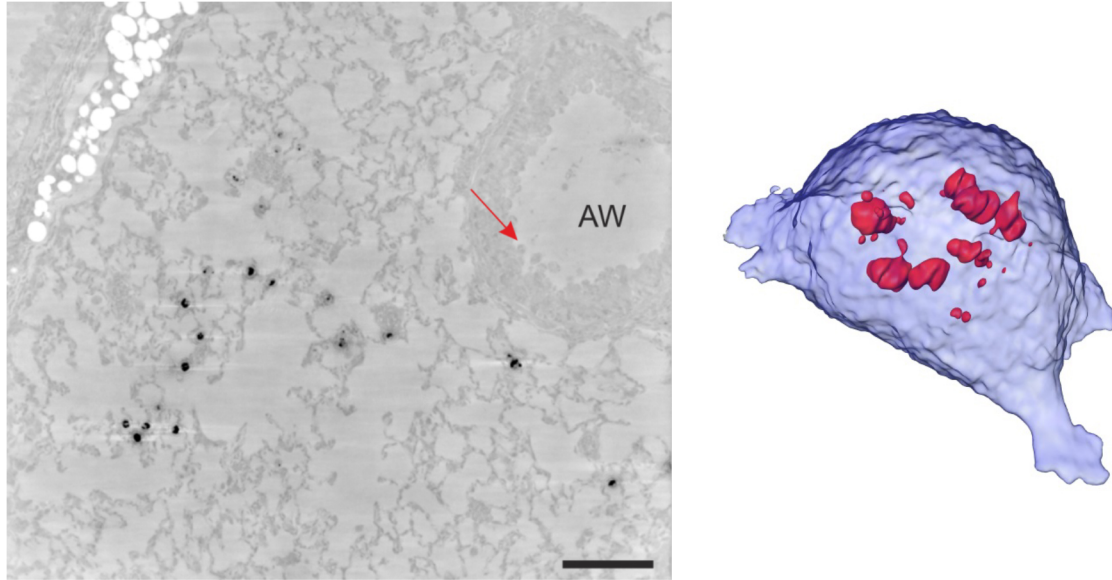


Figure 1: (left) Virtual slice through a 3D volume of an in situ lung slice. Fat (white) and barium-labelled macrophages (black) can be clearly resolved besides the detailed soft tissue structure that even allows to resolve single goblet cells (arrow) protruding the airway (AW). Scale bar denotes 100 μm . (right) 3D Rendering of a single osmium stained macrophage, which was embedded in a 2 mm thick piece of resin. The 3D resolution of the underlying dataset was measured using Fourier shell correlation to be 83 nm.

1.2 Development of microfluidic platforms to study biological matter by x-rays (AG Köster)

Microfluidics is a very well established technique in light microscopy applied by groups from physics, engineering, chemistry, medicine, and biology. Even though the great advantages of microfluidics (such as high time-resolution, superior control of experimental parameters and low sample consumption) are also valid in x-ray studies, the method is not as widely spread, so far. One reason may be that, whereas the fabrication of microfluidic devices for microscopy applications from PDMS (polydimethylsiloxane) and glass is relatively easy and inexpensive, there is no such standard protocol for x-ray applications.

Thus, we have been working towards a versatile microfluidic chip fulfilling the following requirements: (i) x-ray compatibility (low absorption, low background scattering, radiation resistance), (ii) biological inertness, (iii) flexibility in channel design, (iv) reproducibility. In the past year, we have established two different device types in our group. First, a PDMS-quartz capillary composite device has been developed, as shown in Figure 3 (Saldanha, Köster et al., unpublished). The device has been tested for drop production (diameter on the order of 100 μl), into which we encapsulated vimentin

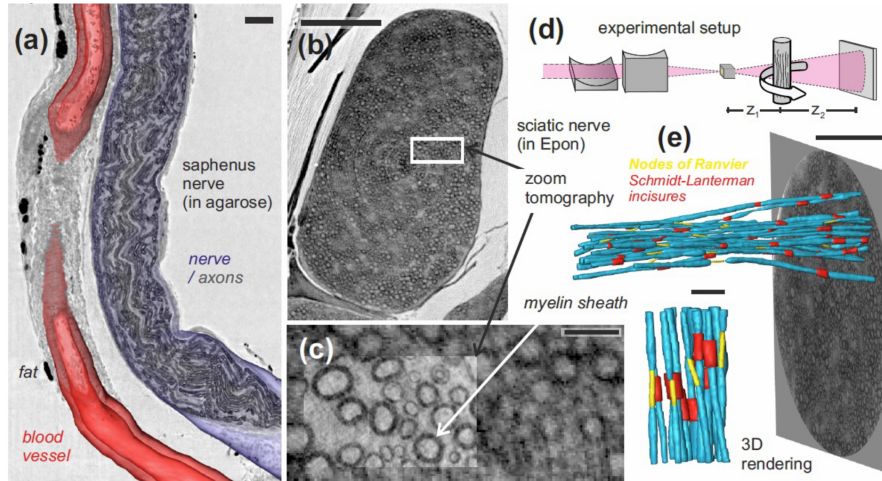


Figure 2: (a) Three-dimensional rendering of a mouse saphenus nerve (blue) with adjacent blood vessel (red) along with a longitudinal virtual slice. The nerve was stained with osmium tetroxide. Scale bar 50 μm . (b) Virtual slice through an EPON-embedded osmium stained sciatic nerve, voxel size 430 nm. Scale bar 100 μm . (c) Magnified view of the region marked in (b) along with data obtained from a zoom-tomogram of the same nerve with 50 nm voxel size. Scale bar 10 μm . (d) Experimental setup: The undulator beam is focused by two elliptically shaped mirrors (KB) and (optionally) filtered by an x-ray waveguide system. The nerve is placed at various distances z_1 from the focus within the divergent (partially) coherent beam and magnified Fresnel diffraction patterns (holograms) are recorded. Subsequent phase retrieval and tomographic reconstruction allows quantitative 3D electron density determination. (e) 3D rendering of a sciatic nerve probed by zoom tomography: (top) view of a 100 nm voxel size dataset is shown along with a virtual slice through the reconstructed volume. Nodes of Ranvier are rendered yellow, Schmidt-Lanterman incisures red. Scale bars 100 μm . (bottom) Rendering of 13 axons, suggesting a correlation between positions of nodes and incisures of neighbouring axons. Scale bar 10 μm .

intermediate filament protein along with assembly buffer (100 mmol KCl in phosphate buffer). By recording the scattering signal from different positions downstream the capillary, we were able to probe different stages (time points) in the assembly process, thus combining high spatial resolution ($q_{\text{max}} \approx 2 \text{ nm}^{-1}$) and high temporal resolution. We used very short exposure times (10 ms) at a high repetition rate (3 ms dead time; possible with the now available Eiger detector from Dectris) to resolve the positions of the oil-water interface precisely and “clean” our signal from the streaks and the oil signal.

The same device was also used for investigation of the scattering pattern from red blood cells (RBCs) as they flow by the beam. This high-throughput technique is a step towards the development of sample environments for FEL (free-electron-laser) applications. Im-

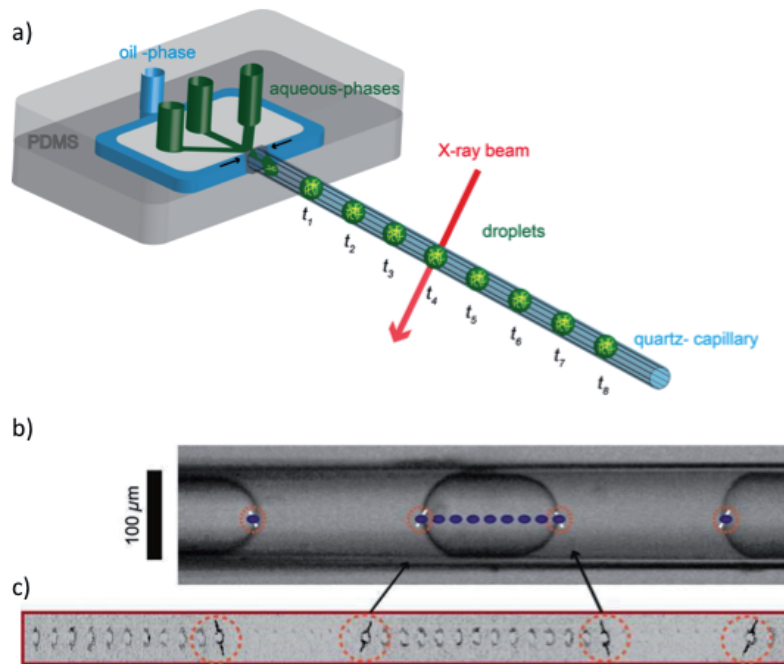


Figure 3: a) Schematic of the composite PDMS-quartz capillary device including one inlet for the oil phase and 3 inlets for aqueous phases, which are mixed and encapsulate monodisperse drops. The drops flow down a quartz capillary and are probed by the x-ray beam (denoted by the red arrow). b) Bright field micrograph of droplet flowing in the capillary and measurement positions marked by blue dots. c) A series of scattering patterns recorded as the drops flow by. We can clearly distinguish the interior of the drops (in this case vimentin intermediate filament protein), the oil and the interface, which leads to streaks.

portantly, these devices are very easy to fabricate, robust (we were able to run the same devices over several days without leakage or breaking) and the PDMS part can be designed to serve different functionalities (e. g., drop production, fast diffusive mixing, delay lines etc.).

Second, Topas COC (cyclic olefin copolymer) devices have been fabricated by hot embossing. Topas is a radiation resistant material with low absorption and low background when thin films are used. The hard plastic can be purchased either as pellets or as films with a predefined thickness. The pellets have to be dissolved in toluene and spin coated in order to achieve thin films. The desired channel geometry is produced by conventional photolithography, Thus virtually any geometry with channel dimensions between about 10 μm and about 500 μm can be realized. The “master structure” consisting of a silicon wafer and a photoresist (typically SU-8) structure is transferred into the Topas by hot embossing, i. e., applying a defined pressure and a defined temperature to the material.

Bonding of a second Topas layer to the structure is performed by the same method. Thus, we achieve a device, which is made completely of the same material. As for the capillary devices, the Topas devices are comparatively easy to fabricate. We plan to perform a few more tests and optimizations during the upcoming beamtimes and will then make the protocol available to the used community.

1.3 Combined ptychography and nano-diffraction for cellular imaging (AG Köster & AG Schroer)

As a collaboration of the Köster and Schroer research groups, we have developed a versatile approach to cellular imaging by x-rays (Figure 4, published in [29]). Cells were grown on silicon-rich nitride windows, chemically fixed and freeze-dried. Ptychography and nanodiffraction measurements were performed at the identical sample position by moving the sample in the beam focus (nano-diffraction, beam size of $100 \times 150 \text{ nm}^2$) and slightly out of focus (ptychography, $850 \times 950 \text{ nm}^2$). Thus we achieved images of the whole cell at a comparatively low dose and were able to identify from these overview images regions of interest (ROI), in which we performed nano-diffraction. The nano-diffraction data provide high-resolution reciprocal space data. We developed a model to quantify structural parameters of the intracellular protein networks/bundles, such as filament diameters, bundle diameters, filament-filament distances and packing geometry of the filaments.

1.4 X-ray nanoprobe analysis of diatoms (AG Rosenhahn)

While in the beginning of the VI our focus was on XRF investigations on barnacle larvae [30, 31], we now attempted the challenging study of much smaller biofouling species. The diatom *Navicula perminuta* is 10–13 μm in length and a marine biofilm forming organism frequently appearing at ship hulls and prevalent on most antifouling coatings [30, 31]. The adhesive of diatoms contains a complex mixture of substances rich in polymers such as polysaccharides or glycoproteins [32]. Within this VI, the inorganic components in the material were analyzed by x-ray nanoprobe fluorescence analysis. The algae were settled on different substrates like silicon nitride membranes or on vacuum compatible Kapton foils and investigated at the ESRF, ANKA, and PETRA III. EDX measurements at an excitation energy of 5 keV showed the presence of chlorine in the adhesive but heavier metals remained undetectable due to the low excitation energy. XRF measurements at the ESRF at the endstation ID16-NI showed the elemental composition of the algae shell, which contains besides Si also Ca, Br, S and Zn (Fig. 5). First measurements after the algae were removed showed also bromine in the very thin adhesive film (around 15 nm).

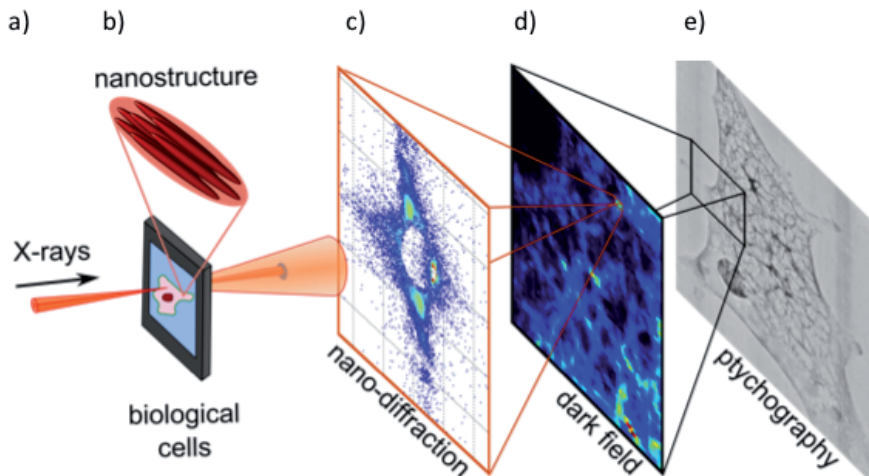


Figure 4: a) Setup of the experiment for combined nano-diffraction and ptychography. b) Schematic of the bundle structure; filament and bundle diameters as well as filament distances can be quantified by our model. c) individual diffraction patterns, from which d) dark field images are computed. e) Ptychogram of the same sample position.

1.5 Biological samples: small angle x-ray scattering resolves internal composition of *E. coli* cells (AG Rosenhahn)

In the past year we explored the application of small angle x-ray scattering as high-throughput tool to classify novel antibiotic modes of action [33]. The beamline P12 BioSAXS at PETRA III features an automated sample changer and allows a rapid analysis of many potential substances. The size range available at PETRA (1 nm – 100 nm) is ideal to identify the relevant changes in bacteria with a principle component analysis. The challenge in developing an analytical model of a whole *E. coli* cell is the variety of internal constituents. In order to develop an analytical model it was necessary to gain information of the entire scattering range including signal originating from the outer shape of the bacteria ($\approx 1 \mu\text{m}$ size). Therefore, we established a cooperation with colleagues from APS, Argonne, USA to access the ultra-small angle scattering (USAXS) regime (1 μm – 1000 nm). The information of the outer shape was captured by USAXS (APS, Argonne, USA) and combined with the internal structure resolved in SAXS (P12, PETRA III), see Figure 6a. Built on this data, a model for major structural components of *E. coli* was developed. It was possible to deduce information on occupied volume, occurrence and average size of the most important intracellular constituents: ribosomes, DNA, and proteins (Fig. 6b and Fig. 6c). Thus SAXS can be used as a complementary method to study the internal bacterial composition. We

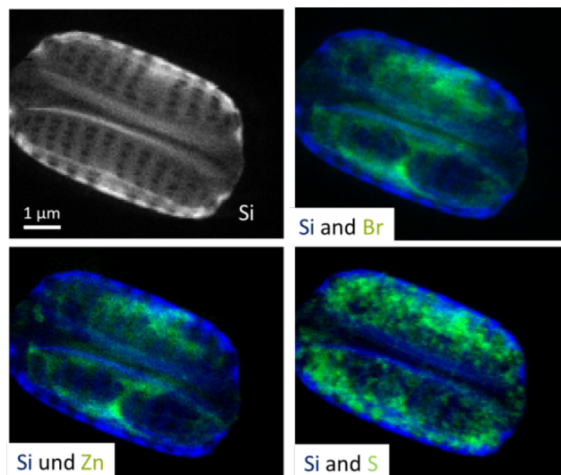


Figure 5: Elemental composition of the algae shell, the scale bar is 1 μm .

studied *E. coli* after treatment with three different antibiotic agents: chloramphenicol, tetracycline, and rifampicin and monitored the impact on the intracellular constituents. The strongest impact of antibiotics was observed on the bacterial DNA. Here, both tetracycline and chloramphenicol led to an aggregation of DNA in the so called ‘nucleoid’ in the center of the bacterial cell (see bright part in Fig. 6d) and thereby reducing the volume occupied by DNA. These observations are in accordance with previous findings by fluorescence microscopy [34] and underscore the potential of SAXS to not only identify novel antibiotic modes of action but to contribute as complementary method for studies of cellular morphology.

1.6 Design of in-situ cell for ptychography and time-resolved imaging of catalyst aging during the sintering process (AG Grunwaldt & AG Schroer)

The development of modern synchrotron radiation techniques, through both instrumentation and theoretical understanding, is gradually enabling the imaging of catalysts at work. In-situ ptychography has benefited from improvement in brilliance and low emittance permitted by modern synchrotron radiation facilities and by improved stability offered by renewed and newly constructed experimental stations. These advances on the experimental side have been paralleled by a steady increase in computing power and the efficiency of reconstruction algorithms, allowing imaging of catalysts under working conditions. Within the virtual institute and in close collaboration with the technical University of Denmark (Ass. Prof. Christian Damsgaard), a new in-situ cell was developed [35] that allows studying catalysts under in-situ conditions and at the same time permits electron microscopic studies. As a relevant system in catalysis and at the same time an excellent model sample, nanoporous gold (np-Au) and $\text{CeO}_2/\text{np-Au}$, were chosen as part

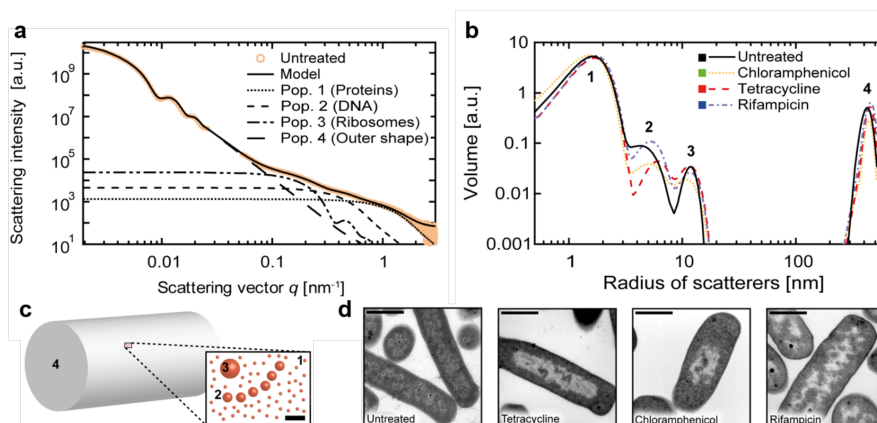


Figure 6: Combined SAXS and USAXS scattering curve of untreated *E. coli*. b) Volume distribution of the cellular components before and after antibiotic treatment c) Illustration of the model featuring a cylinder representing the outer bacterial shape and the major cellular components as spheres. The scale bar has a length of 20 nm. d) TEM images of *E. coli*, the scaling bar has a length of 1 μm .

of a close collaboration with Dr. Arne Wittstock [36] (University of Bremen).

Sample preparation was conducted with a focussed ion beam (FIB) system at the Karlsruhe Nano Micro Facility (KNMF). Our first experiments were conducted as a “proof-of-concept” study and achieved 40 nm spatial resolution at ambient pressure and temperatures up to 600 °C [35]. In additional experiments, we monitored the coarsening and sintering behaviour of np-Au both by environmental electron microscopy and in-situ hard x-ray ptychography. We were able to monitor the sample with a resolution of around 20 nm [37] (cSAXS beamline of the Swiss Light Source, Figure 7). Additionally, we directly measured the temperature using an infrared thermography camera. Pure and CeO₂ coated nanoporous gold (np-Au) was studied around the Ce L_{III} edge (5723 eV). Figure 7 shows some results on the sintering behaviour of the np-Au at various temperature steps in real time under oxidising conditions. Our studies demonstrated that the coarsening of np-Au strongly depends on pressure, temperature, reaction gas atmosphere and potential overlayers.

In a further study, we investigated a core-shell catalyst consisting of a methanol producing core of CuO,ZnO,Al₂O₃ in a ZSM-5 zeolite shell, which promotes methanol dehydration to form dimethyl ether (DME). This was conducted in a close collaboration with Michael Klumpp of the group of Prof. Wilhelm Schwieger (University of Erlangen-Nuremberg). This bi-functional catalyst shifts the chemical equilibrium to the formation of DME and enhances the selectivity to it [38]. Upon activation, the CuO in the methanol forming core is reduced, which leads to a shrinkage of the Cu containing crystallites [39]. We recently performed resonant (Cu K edge, 8979 eV) in-situ ptychography of this complex Cu/ZnO @ ZSM5 core shell catalyst at P06, to study the shrinkage of the core

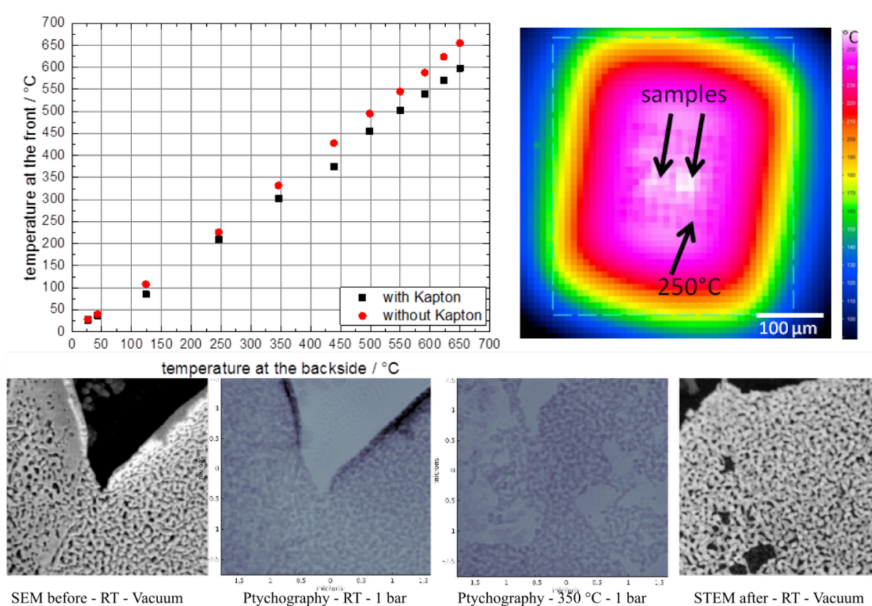


Figure 7: Temperature calibration (top, left) and IR thermography image of the MEMS chip containing a np-Au sample at high temperature (top, right). EM and phase contrast ptychograms of CeO₂/np-Au before, during, and after annealing treatment at different temperatures inside the in-situ cell (bottom).

during redox conditions (Figure 8). Furthermore, the SEM analysis performed before and after the redox treatment allowed us to complement the information on the catalyst behaviour. This shows the convenience and versatility of our design, which allows the same sample chip to be used in transmission electron microscopy and in-situ x-ray microscopy.

One of the main limitations of the present setup is the inability to measure the catalytic activity by means of online mass spectrometry. This is due to the very small amount of catalyst used in the cell with respect to the relatively big gas volume. This limitation is presently being addressed by designing a new generation of in-situ cell with much smaller gas volume. This new system is made possible by 3D printing technology and is

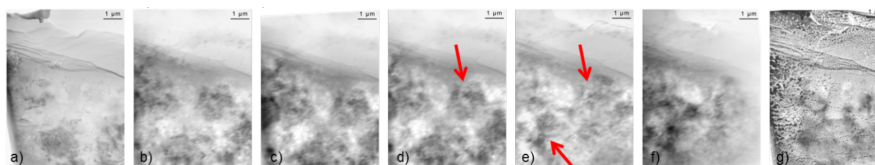


Figure 8: a) Inverted ex-situ BSE-SEM image (vacuum), b-f) in situ ptychograms (phase contrast): b) RT in He, c) 250 °C in H₂, d) 250 °C in O₂, e) 350 °C in H₂, f) 350 °C in O₂, g) inverted ex-situ BSE-SEM image after the in-situ treatment at P06.

presently in the prototype and test stage.

1.7 Application of the new lithographically etched silicon in-situ reactor for 2D study of catalytic reactions: x-ray imaging and spectroscopic studies (AG Grunwaldt)

Understanding the function of catalysts requires knowledge on different length scales. Furthermore, to understand the relationship between structure and activity, it is important to perform studies during the catalytic reaction (in situ). Recently, we described the design and preparation of a novel lithographically etched silicon microreactor [Fig. 9(right)] for combined spectroscopic and imaging studies [4]. The reactor was specifically designed to allow complementary characterization techniques, while supporting a contained gas environment and allowing rapid heating and cooling, due to advantageous heat transfer properties. A central goal was to investigate Catalytic Partial Oxidation (CPO) of methane over heterogeneous platinum catalysts (e. g., Pt/Al₂O₃), taking advantage of the microchannel properties to allow a single catalyst grain (100 – 200 μm) to be observed by scanning or full-field transmission x-ray microscopy. However, the presence of large diffraction peaks on transmission through the silicon body has complicated energy resolved radiography measurements, planned to observe localized ‘hotspot’ formation and Pt-oxidation-state gradients characteristic of the CPO process. Preliminary studies with this new reactor have been performed at ANKA XAS beamline, which show the potential of the system to allow single particle analysis. Slight thermal instabilities were however detected, which disturbed the steady state measurements in situ, as slight variations in temperature are sufficient to move the hotspot and gradient. Further improvements are currently being implemented, including temperature control optimisation and use of alternative materials for the next generation of reactor chips. A further proposed beamtime at P11 later in 2016 is expected to take advantage of these changes to finally achieve this milestone, also with the newly designed lithographically etched silicon in situ reactor (CatRe3).

Despite the issues encountered with imaging and transmission measurements in the microreactor, recent transient temperature investigations during Diesel Oxidation Catalysis (DOC) were successful [40]. In this experiment at ESRF ID24, Pt/Al₂O₃ and Pt-CeO₂/Al₂O₃ catalysts were investigated for their CO oxidation activity during the transient New European Driving Cycle (NEDC), which is a temperature program simulating engine activity in a typical automobile. It requires fast heating and cooling ramps, which cannot be provided by using conventional in-situ reactors. However, due to the high thermal conductivity of the silicon gas phase reactor, very fast heating and cooling can be performed in the gas phase microreactor, which makes it the ideal reactor to be used for transient reactions. Three measurements were performed simultaneously: the catalyst oxidation state by Turbo-XAS, the CO oxidation activity by mass spectrometry, and the formation of oxidation state/thermal gradients by IR thermography. The microreactor was able to successfully reproduce the necessary temperature transients

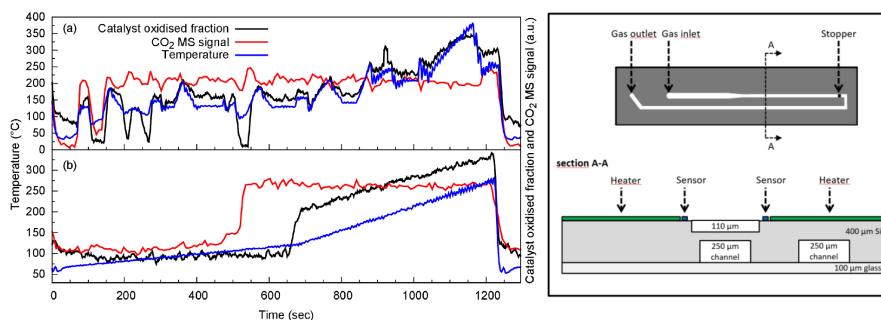


Figure 9: Left: example of NEDC transient temperature cycle, showing temperature profile and catalyst oxidized fraction (calculated by LCA). Right: Schematics of the Si-based microreactor.

[Fig. 9(left)], while data was collected in fluorescence mode. This experiment shows the potential of the microreactor for combined in-situ studies on societally relevant reaction systems. As a synergistic effect of this reactor design, there is a high potential to continue such investigations at DESY, utilizing the capabilities of the upcoming hard XAS and time-resolved spectroscopy beamlines P64 and P65.

1.8 Towards 3D imaging of heterogeneous catalysts: structural changes and reaction gradients observed by in-situ tomography (AG Grunwaldt)

For a complete understanding of the link between catalyst structure and activity in realistic catalyst materials (e. g., honeycombs, powders, plug-flow reactors), it is advantageous to view such materials in 3D by x-ray tomography. Previously, a quasi in situ approach was applied to measure an exhaust gas catalyst monolith, in particular to understand the effect of high-temperature aging on deactivation and sintering of the metal sites [41]. The sintering behaviour could be successfully unravelled on the micrometre scale. This is interesting from an industrial perspective.

This approach is presently further expanded in two directions. Firstly, the quasi in-situ method will be optimised by attempting to image a single specific catalyst particle (BiMoFeCo 4-component oxide) both before and after catalytic testing and high temperature aging. Secondly and in synergy with the previous study, in-situ diffraction tomography measurements are scheduled for an upcoming beamtime at Diamond I18 (April 2016). In this case the bifunctional core-shell catalyst, studied previously by 2D in-situ ptychography (cf. section 1.6, collaboration with Michael Klumpp/Prof. Wilhelm Schwieger) will be examined. The catalyst is intended for use in the one-step synthesis of dimethyl ether (DME), a high value product, from syngas. In a preliminary measurement performed at Diamond, ex-situ 3D images were collected to assess the feasibility of the study (Figure 10, left). This preliminary study showed promising reconstructions

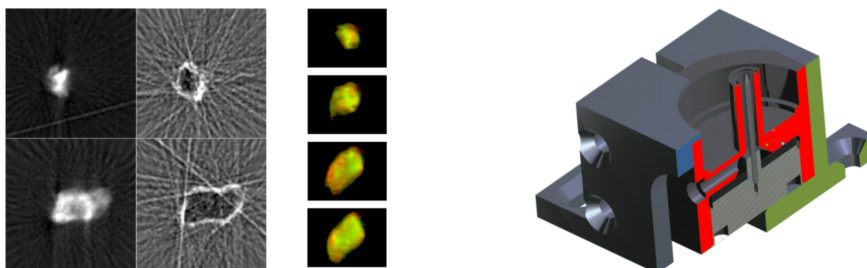


Figure 10: Left: Reconstruction of Cu-Zn based particle slices from preliminary analysis at Diamond light source. Right: Cutaway of the prototype for the new in situ tomography cell.

and a clear elemental distribution including the core/shell border. This study will complement previous 2D investigations (cf. section 1.6), furthermore the observations and insights gained during this experiment will promote the development of our own in-situ tomography apparatus. A new in-situ cell (Figure 10, right) has been designed and will undergo preliminary testing during the next semester. This is expected to be used for full in-situ capabilities in the near future. Therefore, by combining novel in-situ cell design with interesting and relevant catalyst subjects, we expect to make gains towards developing a functional, versatile apparatus and method for 3D tomographic imaging in situ [milestone CatRe5 to be reached in 2016]. These developments may also be adapted to address imaging a single catalyst particle in 3D during CPO of methane [Cat3, 2014], which is so far a work in progress.

1.9 Microfluidic reactor for studies on early stage kinetics and formation of metallic nanoparticles, colloids and precipitates (AG Grunwaldt)

It is highly important to understand and control the intermediate processes occurring during nanoparticle (NP) synthesis. This highlights the necessity for in-situ and operando studies and the combination of complementary characterization techniques (see [42, 43] and [5]). In comparison to conventional stirred batch reactors, production of nanoparticles in continuous flow microreactors has emerged as a promising method, offering several benefits such as homogenous mixing, easy process handling, high mass and heat transport properties and flexible process parameters over a range of operating conditions [44, 45, 46]. A new custom-designed microfluidic setup based on a prototype used previously at PETRA III for a test-beamtime (React2) [47], was designed in order to provide high and pulsation-free flow rates (Figure 11). The microreactor was built up and flow simulations performed in collaboration with the group of Roland Dittmeyer (IMVT, KIT). The reactants are stored in corrosion-resistant vessels and delivered to μ -mixers under pressure of nitrogen to be rapidly and thoroughly mixed.

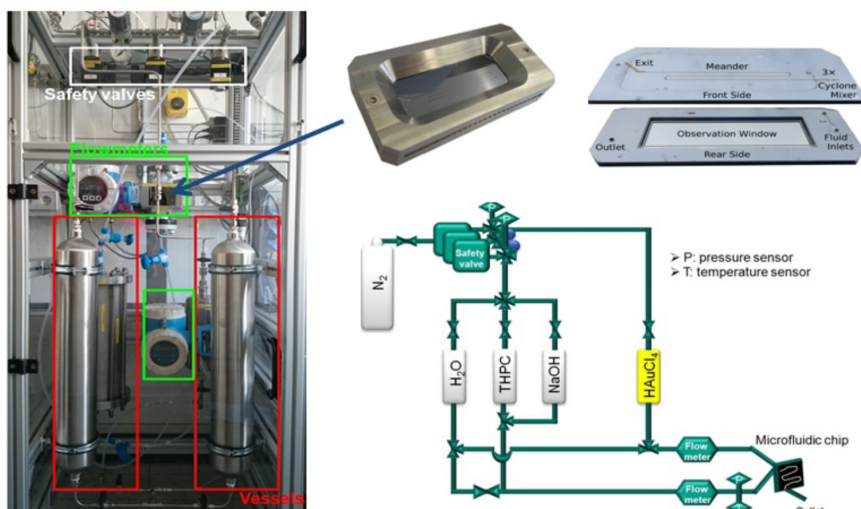


Figure 11: Fluid delivery rack (left); microfluidic chip made of bonded silicon/glass with $300 \times 300 \mu\text{m}^2$ microchannel and assembled stainless steel support (top right); schematic of the setup (bottom right).

The Si-based liquid phase chip contains three cyclone mixers followed by a meandering channel ($300 \times 300 \mu\text{m}^2$) serving as the observation line (Figure 11, top right). It is sandwiched inside a stainless steel frame with access to inlet and outlet ports and including an x-ray transparent observation window. During an initial test beamtime, the formation of gold colloids was found to be strongly dependent on the aging time, concentration, pH etc.

Hence, the setup has been both improved and was tested ‘offline’ in order to optimize the operating parameters for Au-NP synthesis. The produced Au NP colloids were analysed by UV-vis spectroscopy and ex situ by XAS (Figure 12). The results show the formation of stable Au NPs with a desirable particle size (1 – 3 nm). These studies give the basis to obtain further insights into the early stage of Au nanoparticle formation as a function of flow rates, reducing agent, concentration of reactants and pH. In parallel, the precipitation of Cu and Zn for the application as a methanol synthesis catalyst has been studied first in a batch reactor and will now be extended to the microfluidic reactor.

1.10 Morphological analysis of ceriumoxide stabilized nanoporous gold catalysts with resonant soft x-ray scattering (AG Rosenhahn & AG Grunwaldt)

In a collaboration of AG Rosenhahn and AG Grunwaldt, anomalous soft x-ray scattering was applied to nanoporous gold catalysts. Nanoporous gold [36] is a promising catalyst

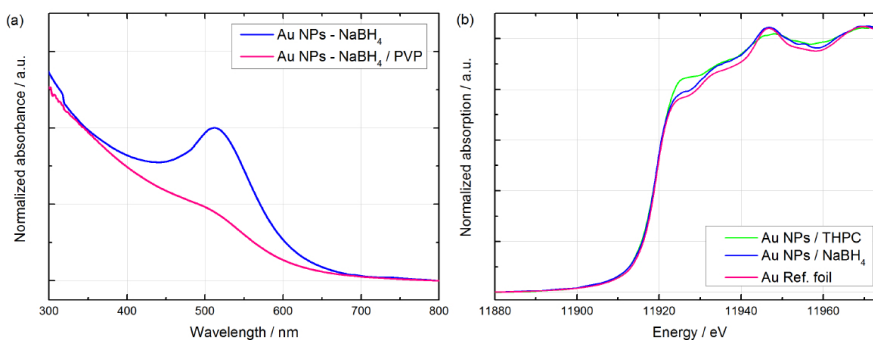


Figure 12: a) UV-vis spectra of Au NPs produced in μ -fluidic device with and without PVP surfactant, (b) XAS spectra of Au NPs produced by different reducing agents.

material for industrial applications that enables selective oxidation reaction of methanol towards methylformate. Especially the addition of cerium oxide nanoparticles (CeO_x) promises enhanced morphological stability during high-temperature applications as a coarsening of the catalyst material leads to a loss of catalytic activity. In this context, x-ray nanoanalysis is of particular relevance as the high penetration depth allows to study bulk catalyst material with high spatial resolution. We applied soft x-ray small angle x-ray scattering (SAXS) using the soft x-ray scattering chamber HORST to determine temperature induced structural changes in nanoporous gold catalysts. The results show that CeO_x deposits enhance the temperature stability of the nanoporous gold catalyst (Figure 13a and b). In addition we demonstrate the ability of soft x-rays to selectively provide structural information on the stabilizing cerium oxide deposits via resonant, anomalous SAXS (ASAXS) measurements at the cerium M edge (Figure 13c).

1.11 In-situ x-ray diffraction studies of structural evolution of colloidal crystal films formed by polystyrene spherical particles upon heating (AG Vartanyants)

In the frame of our VI we performed in situ x-ray diffraction studies of the structural evolution of colloidal crystal films formed by polystyrene spherical particles upon incremental heating [see Fig. 14(top left)]. The experiment was performed at the coherence beamline P10 at PETRA III. The Bragg peak parameters, such as peak position, integrated intensity, and radial and azimuthal widths were analyzed as a function of temperature. A quantitative study of colloidal crystal lattice distortions and mosaic spread as a function of temperature was carried out using Williamson-Hall plots based on a mosaic block model. The temperature dependence of the diameter of the polystyrene particles was obtained from the analysis of Bragg peaks, and the form factor contribution extracted from the diffraction patterns. Four stages of structural evolution in a colloidal crystal upon heating were identified. Based on this analysis, a model of the heating and melting process in the colloidal crystal film is suggested [see Fig. 14(bottom-left)].

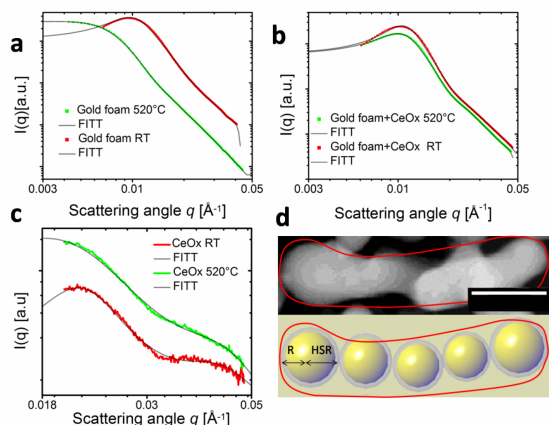


Figure 13: SAXS data of a pure nanoporous gold foam catalyst before (a) and after (b) treatment with CeO_x particles. The addition of CeO_x prevents the gold foam from coarsening (b). (c) ASAXS data of cerium oxide nanoparticles was obtained at the cerium M edge. (d) Schematic representation of the model for the foam-like catalyst structure. The 3D gold foam structure was modeled as chains of globular Au nanoparticles. The length of the scaling bar is 2000 \AA .

Results of this research were published in Langmuir [6] and were highlighted on the cover page [see Fig. 14(right)].

We further developed the method of angular x-ray cross-correlation analysis (XCCA) by applying it to polymer films [7] as well as to liquid crystals [8]. Experiments were performed at P10 at PETRA III using also nano-focusing set up GINIX developed by AG Salditt.

The hidden structural properties of semicrystalline polymer films were revealed by nanofocused x-ray scattering studies [7]. XCCA was employed for the analysis of diffraction patterns from blends of poly(3-hexylthiophene) (P3HT) with gold nanoparticles (AuNPs) [see Fig. 15i)]. Spatially resolved maps of the orientational distribution of crystalline domains allow us to distinguish sample regions of predominant face-on morphology, with a continuous transition to edge-on morphology [see Fig. 15ii)]. The average size of crystalline domains was determined to be of the order of 10 nm. As compared to pristine P3HT film, the P3HT/AuNPs blend is characterized by substantial ordering of crystalline domains, which can be induced by Au nanoparticles. The inhomogeneous structure of the polymer film is clearly visualized on the spatially resolved nanoscale 2D maps obtained using XCCA. Our results suggest that the observed changes of the polymer matrix within crystalline regions can be attributed to nanoconfinement in the presence of gold nanoparticles.

We performed an x-ray study of freely suspended hexatic films of the liquid crystal 3(10)OBC [8]. Our results reveal spatial inhomogeneities of the bond-orientational

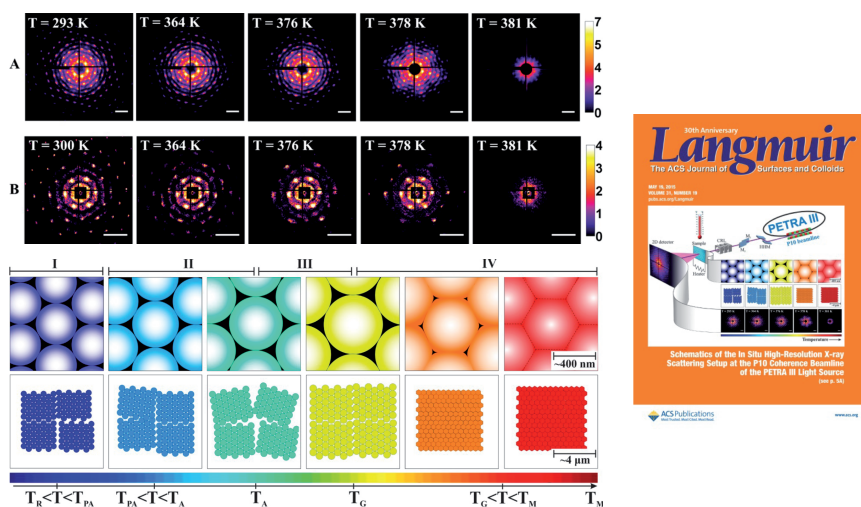


Figure 14: (upper left) X-ray diffraction patterns measured in situ during incremental heating of the PS colloidal crystals in experiments A and B (see text for details). Intensity values are presented in logarithmic color scale. Scale bar shown for each pattern is $50 \mu\text{m}^{-1}$. (lower left) Schematic diagram of the structural evolution in a colloidal crystal film under incremental heating at nanoscopic (top row) and mesoscopic (bottom row) length scales. (right) Cover page of Langmuir.

(BO) order in the vicinity of the hexatic-smectic phase transition and the formation of large-scale hexatic domains at lower temperatures. Deep in the hexatic phase up to 25 successive sixfold BO order parameters have been directly determined by means of XCCA. Such strongly developed hexatic order allowed us to determine higher order correction terms in the scaling relation predicted by the multicritical scaling theory over a full temperature range of the hexatic phase existence.

1.12 Soft x-ray ptychographic imaging of diatoms (AG Vartayants & AG Rosenhahn)

As a collaboration of AG Vartayants and AG Rosenhahn, we performed water-window ptychographic imaging with characterized coherent x-rays at the beamline P04 of the PETRA III [9]. A ptychographical coherent diffractive imaging experiment in the water window with focused soft x-rays at 500 eV is reported. The beam coherence was measured with the newly developed non-redundant array method, and a coherence length of $4.1 \mu\text{m}$ and global degree of coherence of 35% at $100 \mu\text{m}$ exit-slit opening in the vertical direction were determined. A pinhole, $2.6 \mu\text{m}$ in size, selected the coherent part of the beam that was used to obtain ptychographic reconstruction results of a lithographically manufactured test sample and a fossil diatom (see Fig. 16). The resolution of 53 nm

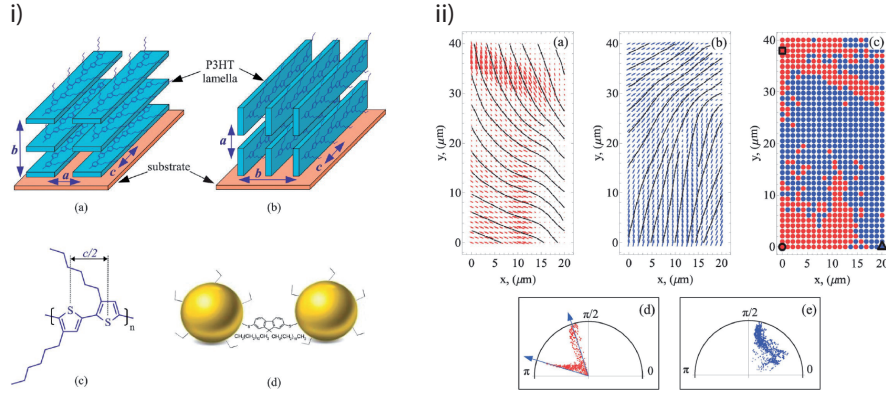


Figure 15: i) Two types of predominant orientation of semicrystalline P3HT domains with respect to a substrate, the face-on (a) and edge-on (b) orientations. (c) Repeating unit of the P3HT polymer chain. (d) Gold nanoparticles stabilized with fluorene derivatives (AuNPs-SFL). ii) Spatial distribution of orientations of crystalline P3HT domains across the film. Each vector in the plotted vector fields corresponds to a certain position on the sample, with the vector length proportional to the modulus of the respective Fourier component. Black lines are plotted to guide the eye. (c) Two sample areas with predominant face-on (red points) and mixed (blue points) orientation of crystalline domains. Angular distribution of all observed orientations in the vector fields (a) and (b) is shown in polar coordinates in (d) and (e), respectively. Arrows in (d) specify two major in-plane orientations of the face-on domains in the sample.

was achieved for the test sample and was only limited by the size of the detector. The diatom was imaged at a resolution better than 90 nm.

1.13 Strain mapping in core-shell nanowires by coherent x-ray diffraction imaging (AG Vartanyants & AG Schroer)

In the frame of VI we performed also a series of strain mapping, coherent x-ray diffraction imaging (CXDI) and ptychography imaging experiments at the nanoprobe station of beamline P06 at PETRA III [10, 11, 12]. Strained InGaN/GaN core-shell nanowires

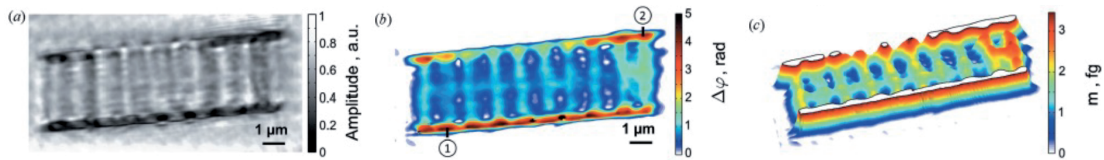


Figure 16: Ptychographic reconstruction of the amplitude (a) and the phase (b) of the fossil diatom. (c) Integrated SiO_2 mass along the depth of the diatom.

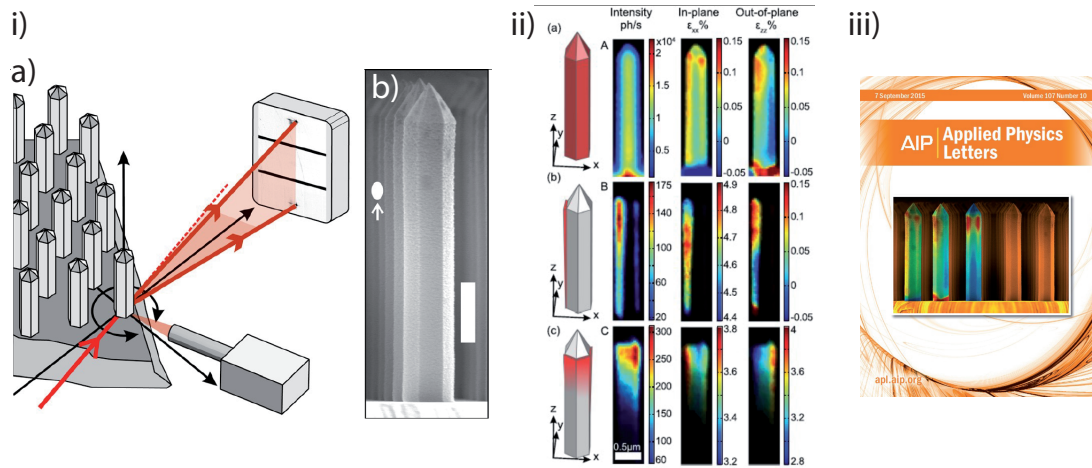


Figure 17: i) Experimental geometry (a) used for SXDM. A single NW at the corner of the sample was positioned in the focus of the x-ray beam and scanned in the xz plane at different ω angles. (b) SEM image of the NW. The white ellipse represents the FWHM of the incident beam. ii) Intensity and strain maps of the NW sample. The sketches in the left column show the regions of the NW that contribute to the corresponding maps. Region A corresponds to the GaN core. Region B corresponds to the strained InGaN shell. From the intensity map of region B, we can see that it mostly contributes to the left side of the shell. Values of the strain component ε_{zz} are continuous between the left side of the shell and the left side of the GaN core, meaning that the growth is pseudomorphic. Region C corresponds to the relaxed part of the InGaN shell on the right and top parts of the NW. iii) Cover page of Appl. Phys. Lett..

(NWs) are promising candidates for solid state lighting applications due to their superior properties compared to planar films. NW based devices consist of multiple functional layers, which sum up to many hundred nanometers in thickness, that can uniquely be accessed in a non-destructive fashion by hard x-rays. A detailed nanoscale strain mapping was performed on a single, 400 nm thick and 2 μm long core-shell InGaN/GaN nanowire with an x-ray beam focused down to 100 nm [10] [see Fig. 17i)]. We observe an inhomogeneous strain distribution caused by the asymmetric strain relaxation in the shell. One side of the InGaN shell was fully strained, whereas the other side and the top part were relaxed. Additionally, tilt and strain gradients were determined at the interface with the substrate [Fig. 17ii)]. Results of this work were highlighted on the cover page of Applied Physics Letters [Fig. 17iii)].

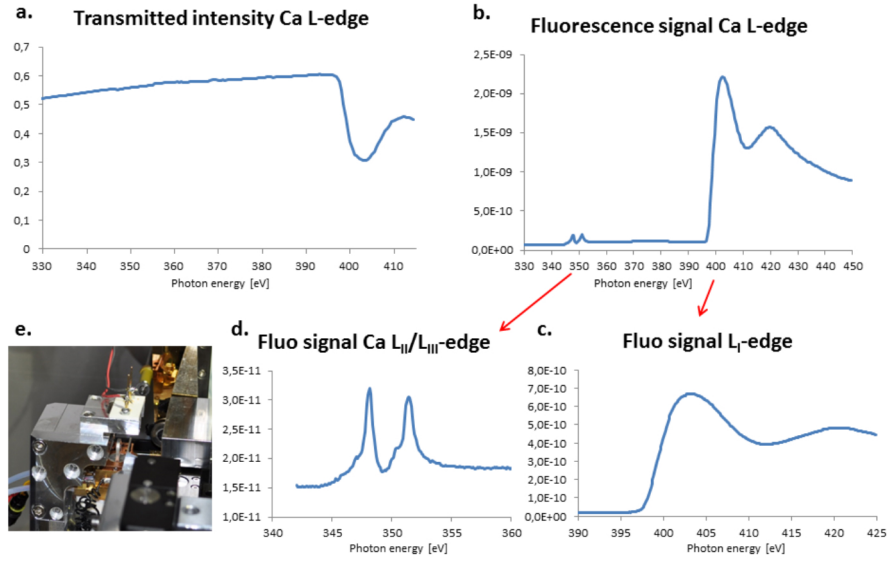


Figure 18: X-ray absorption spectra of $\text{Ca}_3(\text{PO}_4)_2$ measured at the Ca L edge. Direct measurement of the transmitted intensity reveals only the increased absorption above the dominant L_I edge (a). A measurement of the total yield fluorescence signal (b) obtained from the same sample under identical conditions reveals not only the L_I edge (c), but also the L_{II} and L_{III} edges (d). The large sensitive area of the photo diode (1 cm^2) and the close proximity to the sample ensures an efficient detection of the integrated fluorescence signal.

1.14 Implementation of a total fluorescence yield NEXAFS mode for HORST (AG Rosenhahn)

Our versatile x-ray scattering chamber HORST received an upgrade of its spectroscopic capabilities. Although x-ray spectroscopy is not a main application of the setup, the ability to perform basic spectroscopic measurements is a prerequisite for successful imaging experiments exploiting the intrinsic chemical contrast at various x-ray absorption edges in the soft x-ray regime [48]. Until now, x-ray absorption spectroscopy (XAS) with HORST could only be performed by measuring the transmitted intensity using a photodiode placed behind the sample. A new, recently implemented photodiode is placed in very close distance to the sample, oriented perpendicularly to the excitation beam. This configuration ensures that mainly x-ray fluorescence photons are detected. By comparing the directly measured transmission spectrum of a thin layer of $\text{Ca}_3(\text{PO}_4)_2$ at the Ca L edge (Figure 18a) with fluorescence signal measurements of the same sample (Figure 18b-d), the advantage of the latter method in terms of increased sensitivity for minor spectral features is illustrated. Measurements using the fluorescence photo diode should in principle be fully compatible with the cryogenic sample stage (Figure 18e), opening up the possibility of sensitive XAS experiments with frozen-hydrated specimens.

1.15 X-ray microscope at beamline P11 (AG Meents)

Most parts of the combined full-field and scanning microscope to be installed at beamline P11 have been built and successfully commissioned during the last year. Only for the cryogenic sample cooling and loading technical challenges lead to a further delay of the microscope. 3D experiments at cryogenic temperatures using the setup could therefore not be performed yet.

In addition further high-resolution x-ray microscopy experiments were performed from both artificial test samples and biological tissue sections labelled with gold nanoclusters. For the second half of 2016 two first user experiments using the Zernike phase contrast setup are foreseen.

2 Erreichte Meilensteine

In the following, we discuss the progress and comment on the individual milestones:

Mem4 (year 4) These experiments were postponed (milestone not reached in 2015).

Cell4 (year 4) Experiments on (initially) living cells (milestone reached).

Alg4 (year 4) Chemical imaging of biofouling organisms, as shown in section 1.4 (milestone reached).

Sin4 (year 4) Time-resolved imaging of aging during the sintering process has been achieved on nanoporous gold and nanostructured catalysts; collaborations with Arne Wittstock (University of Bremen), Christian Damsgaard (Technical University of Denmark) and Wilhelm Schwieger have been successfully conducted (milestone reached).

React4 (year 4) The study on mechanisms of precipitation reaction using XAS, SAXS and XRD from the formation of clusters towards larger aggregates, e. g., copper-based catalysts for methanol synthesis has been started but needs an additional year to be realized due to the much more complex setup of the microreactor to avoiding the pulsing (milestone not reached).

Mfluid3 (year 3) Microfluidic devices for use in beamlines P06 have been further improved. Temperature control in case of gas-phase reactions in catalysis and pulsation free-flow under turbulent mixing conditions for the preparation of colloids and solids are a much bigger challenge than originally anticipated (milestone partially reached, further work in progress).

CatRe3 (year 3) In-situ reactor for 2D study of catalytic reactions has been further improved and also exploited for other projects, e. g., time-resolved studies (milestone partially reached, further work in progress).

Cell5 (year 5) Platform for conducting cell experiments including data analysis established (also offered to beamline users).

Mfluid5 (year 5) microfluidic platforms, which can be applied (also by beamline users) to a variety of chemical and biological experiments.

Mdiff5 (year 5) With limitations (no cryogenic samples measurements) this milestone Mdiff5 has been reached and the setup is now available to the users.

Mem3b (year 3) cf. section 1.1 (milestone reached).

3 Einhaltung des Finanzierungs- und Zeitplans

Currently, the project is within the financial and time plan. We have applied for a project extension without additional cost due to maternal leaves at KIT and TU Dresden.

4 Publikationen, Vorträge, Preise etc. bitte gegebenenfalls als Anhang beifügen

4.1 Berufung:

In 2015, Hudson W. P. Carvalho (KIT) was appointed Asst. Prof. in Applied Spectroscopy for the Study of Nanomaterials in Agriculture and Environment at the University of São Paulo.

4.2 Meetings & Outreach into the Scientific Community:

The international x-ray absorption conference XAFS16 was organized in Karlsruhe with Jan-Dierk Grunwaldt as chair person [49]. A special session was dedicated to spatially resolved XAS and x-ray microscopy and organized by Gerald Falkenberg, Anna Zimina, and Christian Schroer with Koen Janssens as keynote speaker. Session chairs were Christian G. Schroer, Gerald Falkenberg, Axel Rosenhahn and Ulrike Boesenberg (www.xafs16.org). In addition, x-ray microscopy was also one of the topics of the “Sino-German Workshop on Catalysis and Membranes” (August 28 – 29, 2015, Karlsruhe).

A satellite workshop to the DESY Photon Science Users Meeting in Hamburg was organized by the VI-403. It is already the 5th workshop held in the context of the Users Meeting entitled “5th Workshop on X-Ray Nano-Imaging of Biological and Chemical Systems at PETRA III”. It aimed at the Photon Science user community interested in nano imaging, giving an overview over the possibilities of nano imaging at the x-ray

microscopes at PETRA III (cf. group photo below). Users presented their recent results. The workshop was well attended with over 80 participants.



4.3 Oral Presentations:

- S. Köster, European Biophysics Congress (EBSA), Dresden, Germany
- S. Köster, Gordon Research Conference “Physics and Chemistry of Microfluidics”, Vermont, USA
- C. G. Schroer, “PETRA IV Opportunities for Imaging”, PETRA IV Science Workshop, DESY, Hamburg, Germany, March 23, 2015
- S. Köster, “Local imaging of biological systems — linking structure and function”, PETRA IV Science Workshop, DESY, Hamburg, Germany, March 23, 2015
- T. Salditt, “From 3D to 4D nanoscale coherent imaging”, PETRA IV Science Workshop, DESY, Hamburg, Germany, March 23, 2015
- I. Vartanyants, “Coherent X-ray Imaging of Crystals with Atomic Resolution at Diffraction Limited Sources”, PETRA IV Science Workshop, DESY, Hamburg, Germany, March 23, 2015
- S. Köster, Early Science Workshop @ MID/XFEL, Hamburg, Germany
- S. Köster, LMU München, 26. October 2015
- S. Köster, Universität Hamburg, 27. October 2015

- S. Köster, Universität Greifswald, 2. July 2015
- A. Meents, “Flexible Focusing Optics at beamline P11 at PETRA III”, 2nd German-Swedish Workshop on Synchrotron Optics, Berlin, 30. April, 2015.
- A. Meents, “Future detector needs for protein crystallography”, 7th International workshop on Radiation Imaging Detectors, IWORID 17, Hamburg, 01. July, 2015.
- S. Baier, “In situ ptychography during the annealing treatment of heterogeneous nanoporous gold catalysts”, 5th International Conference on Operando Spectroscopy, Deauville, France, May 17, 2015 – May 21, 2015
- S. Baier, “Lithographically fabricated silicon microreactor for in situ characterization of heterogeneous catalysts”, 16th International Conference on X-ray Absorption Fine Structure, 23-28 August 2015, Karlsruhe, Germany
- A. Gänzler, O. Muller, M. Casapu, R. Frahm, J.-D. Grunwaldt, “Operando structure-activity correlations in applied catalytic systems: Oscillatory CO oxidation in exhaust gas catalysts”, 16th International Conference on X-ray Absorption Fine Structure, 23-28 August 2015, Karlsruhe, Germany
- S. Baier, “Application of X-ray microscopy and ptychography in heterogeneous catalysis”, DESY Photon Science Users’ Meeting, European XFEL Users’ Meeting, 28 – 30.01.2015
- D. E. Doronkin, “Operando spatially- and time-resolved XAS and valence-to-core XES for the characterization of Fe- and Cu-Zeolite catalysts for NH₃-SCR of NO_x”, Europacat XII, 30.08 - 4.09.2015
- J.-D. Grunwaldt, “Probing the structure of catalysts at work by advanced X-ray techniques”, ISHHC 17, Utrecht, The Netherlands, 12.-15.07.2015 (invited keynote lecture)
- D.E. Doronkin, “Operando Spatially- and Time-Resolved XAS and Valence-to-Core-Xes to Study the Mechanism of the NH₃-SCR over Fe- and Cu-Zeolites”, NAM24, June 14-19, 2015, Pittsburgh, PA, USA
- J.-D. Grunwaldt, “Probing the structure of catalysts at work by advanced X-ray techniques”, Shanghai Synchrotron Radiation Facility Seminar, 26.09.2015
- J.-D. Grunwaldt, “Knowledge-based catalyst design and operando spectroscopy: Case studies from oxidation and exhaust gas catalysis”, Seminar at State Key Laboratory of Catalysis, DCIP, Dalian, 25.09.2015
- J.-D. Grunwaldt, “Exhaust gas catalysts in action: Advanced preparation methods and novel insight into their structure”, Institute Seminar, Department of Chemical and Biochemical Engineering, Technical University of Denmark, Kgs. Lyngby, Sept. 16, 2015

- J.-D. Grunwaldt, “Imaging nanomaterials and catalysts at work: A great challenge for hard X-rays”, PSC Road Map Symposium, DESY, Hamburg, May 6, 2015
- J.-D. Grunwaldt, “Catalyst design, operando spectroscopy and application in oxidation and exhaust gas catalysis”, Fritz-Haber-Institute, Berlin, April 29, 2015
- J.-D. Grunwaldt, “Design, application and dynamics in oxidation and exhaust gas catalysis”, IRCELYON, Lyon, April 9, 2015
- J.-D. Grunwaldt, “Nanomaterials in catalysis – a challenge for chemical imaging”, Workshop “science at PETRA IV” at DESY, Hamburg, March 23 - 24, 2015 (invited)
- C. G. Schroer, “Kristallographie des Nichtkristallinen: Mikroskopie mit kohärenter Röntgenstrahlung”, Physikkolloquium, TU Dresden, May 5, 2015.
- C. G. Schroer, “Pushing the Limits of Hard X-Ray Coherent Diffraction Imaging”, ICXOM2015, Brookhaven, NY, USA, Sept. 15, 2015 (invited)
- C. G. Schroer, “Hard X-Ray Scanning Microscopes Based on Refractive Optics”, SRI2015, New York, NY, USA, July 8, 2015
- C. G. Schroer, “XFEL Science with Nanobeams”, MID Workshop, European XFEL, Hamburg, Jan. 26, 2015
- J. Patommel, “Refraktive Röntgenlinsen aus Lamellen konstanter Dicke”, DPG Tagung, Berlin, March 18, 2015
- C. G. Schroer, “X-Ray Nano-Imaging of Biological and Chemical Systems at PETRA III”, 5th Workshop on X-Ray Nano-Imaging of Biological and Chemical Systems at PETRA III, DESY Users’ Meeting, Jan. 29, 2015

4.4 Technology Transfer

The DESY spin-off company suna-precision has sold several low-background sample holders from single crystalline silicon, which were developed in the framework of VI-403. License agreements with DESY are currently negotiated. Further products such as the x-ray microscopy scanning stage are foreseen to be commercialized and licensed in 2016.

4.5 International Collaborations

Within the activities of the VI the following international collaborations have been established:

- John Miao, UCLA (photoinduced chemical reactions)

- Florian Meirer, Utrecht (tomography of catalytic particles)
- Dimitrov Orlov, Lund (tomography of precipitates in light metals)
- Magdalena Sczerbowska-Boruchowska, Krakov (x-ray microscopy of medical tissues)
- Danielle Pellicia, Melbourne (tomography, fluorescence imaging)
- Jesper Wallentin, Lund (in operando studies of nanowires)
- Ulrich Vogt, KTH Stockholm (x-ray nanooptics)
- Christian Damsgaard, DTU Copenhagen (in-situ cells for imaging catalysts)
- Robert Feidenhansl', Niels Bohr Institute, University of Copenhagen, Copenhagen (Nanowires)
- Advanced Photon Source, Argonne, IL, USA (USAXS on bacteria)
- Shubnikov Institute of Crystallography RAS, Moscow Russia (x-ray physics)
- Van 't Hoff laboratory for Physical and Colloid Chemistry, Debye Institute for Nanomaterials Science, Utrecht University (colloidal systems)
- National Research Nuclear University MEPhI (Moscow Engineering Physics Institute), Moscow, Russia (x-ray physics)
- NRC "Kurchatov Institute", Moscow, Russia (x-ray physics)
- A. Singer, University of California San Diego, La Jolla, California, United States (coherent x-ray imaging techniques)
- National Research Tomsk Polytechnic University (TPU), Tomsk, Russia
- Department of Chemistry and Center for Nanotechnology for Engineering (CNIS), University of Rome Sapienza, Rome, Italy
- Landau Institute for Theoretical Physics, Russian Academy of Sciences, Chernogolovka, Russia
- Moscow Institute of Physics and Technology (State University), Dolgoprudny, Russia
- Skobeltsyn Institute of Nuclear Physics, Lomonosov Moscow State University, Moscow, Russia
- NanoLund, Department of Physics, Lund University, Lund, Sweden

4.6 Outreach

- S. Köster, Course on Modeling Cellular Systems in Space and Time, Poquerolles, France
- C. G. Schroer, “X-Ray Microscopy & Tomography: Sharp Views into the Nano Cosmos”, RACIRI School, Rügen, Germany, Aug. 25, 2015

Publications in the Reporting Period

- [1] M. Bartels, M. Krenkel, J. Haber, R. N. Wilke, and T. Salditt, *Phys. Rev. Lett.* **114**, 048103 (2015).
- [2] M. Krenkel, A. Markus, M. Bartels, C. Dullin, F. Alves, and T. Salditt, *Scientific Reports* **5**, 09973 (2015).
- [3] M. Bartels, M. Krenkel, P. Cloetens, W. Möbius, and T. Salditt, *J. Struct. Bio.* **192**, 561 (2015).
- [4] S. Baier, A. Rochet, G. Hofmann, M. Kraut, and J.-D. Grunwaldt, *Rev. Sci. Instrum.* **86**, 065101 (2015).
- [5] A. Gänzler, M. Casapu, A. Boubnov, O. Müller, S. Conrad, H. Lichtenberg, R. Frahm, and J.-D. Grunwaldt, *J. Catal.* **328**, 216 (2015).
- [6] E. A. Sulyanova, A. Shabalin, A. V. Zozulya, J.-M. Meijer, D. Dzhigaev, O. Gorobtsov, R. P. Kurta, S. Lazarev, U. Lorenz, A. Singer, O. Yefanov, I. Zaluzhnyy, I. Besedin, M. Sprung, A. V. Petukhov, and I. A. Vartanyants, *Langmuir* **31**, 5274 (2015).
- [7] R. P. Kurta, L. Grodd, E. Mikayelyan, O. Y. Gorobtsov, I. A. Zaluzhnyy, I. Fratoddi, I. Venditti, M. V. Russo, M. Sprung, I. A. Vartanyants, and S. Grigorian, *Phys. Chem. Chem. Phys.* **17**, 7404 (2015).
- [8] I. A. Zaluzhnyy, R. P. Kurta, E. A. Sulyanova, O. Y. Gorobtsov, A. G. Shabalin, A. V. Zozulya, A. P. Menushenkov, M. Sprung, B. I. Ostrovskii, and I. A. Vartanyants, *Phys. Rev. E* **91**, 042506 (2015).
- [9] M. Rose, P. Skopintsev, D. Dzhigaev, O. Gorobtsov, T. Senkbeil, A. von Gundlach, T. Gorniak, A. Shabalin, J. Viefhaus, A. Rosenhahn, and I. Vartanyants, *J. Synchrotron Rad.* **22**, 819 (2015).
- [10] T. Stankevič, D. Dzhigaev, Z. Bi, M. Rose, A. Shabalin, J. Reinhardt, A. Mikkelsen, L. Samuelson, G. Falkenberg, I. A. Vartanyants, and R. Feidenhans'l, *Appl. Phys. Lett.* **107**, 103101 (2015).

- [11] T. Stankevič, D. Dzhigaev, Z. Bi, M. Rose, A. Shabalin, J. Reinhardt, A. Mikkelsen, L. Samuelson, G. Falkenberg, I. A. Vartanyants, and R. Feidenhans'l, Proc. SPIE **9592**, 95920D (2015).
- [12] D. Dzhigaev, T. Stankevič, I. Besedin, S. Lazarev, A. Shabalin, M. N. Strikhanov, R. Feidenhans'l, and I. A. Vartanyants, Proc. SPIE **9592**, 95920S (2015).
- [13] R. N. Wilke, N. Quéric, M. Hoppert, C. Heller, A. Schropp, C. G. Schroer, M. Burghammer, T. Salditt, and J. Reitner, Geomicrobiology Journal **32**, 380 (2015).
- [14] C. Dullin, S. dal Monego, E. Larsson, S. Mohammadi, M. Krenkel, C. Garrovo, S. Biffi, A. Lorenzon, A. Markus, J. Napp, T. Salditt, A. Accardo, F. Alvesh, and G. Tromba, J. Synchrotron Rad. **22**, 143 (2015).
- [15] R. N. Wilke, M. Hoppert, M. Krenkel, M. Bartels, and T. Salditt, J. Appl. Cryst. **48**, 465 (2015).
- [16] Z. Huang, M. Bartels, R. Xu, M. Osterhoff, S. Kalbfleisch, M. Sprung, A. Suzuki, Y. Takahashi, T. Blanton, T. Salditt, and J. Miao, Nature Materials **14**, 691 (2015).
- [17] J. Wallentin, R. N. Wilke, M. Osterhoff, and T. Salditt, J. Appl. Cryst. **48**, 1818 (2015).
- [18] M. Töpperwien, M. Priebe, and T. Salditt, Eur. Biophys. J. (2015), doi 10.1007/s00249-015-1107-9.
- [19] T. Salditt, M. Osterhoff, M. Krenkel, R. N. Wilke, M. Priebe, M. Bartels, S. Kalbfleisch, and M. Sprung, J. Synchrotron Rad. **22**, 867 (2015).
- [20] G. Hofmann, A. Rochet, E. Ogel, M. Casapu, S. Ritter, M. Ogurreck, and J.-D. Grunwaldt, RSC Adv. **5**, 6893 (2015).
- [21] C. Y. J. Hémonnot, M. Mauermann, H. Herrmann, and S. Köster, Biomacromolecules **16**, 3313 (2015).
- [22] C. Rossner, O. Glatter, O. Saldanha, S. Köster, and P. Vana, Langmuir **31**, 10573 (2015).
- [23] S. A. Bobkov, A. B. Teslyuk, R. P. Kurta, O. Y. Gorobtsov, O. M. Yefanov, V. A. Ilyin, R. A. Senina, and I. A. Vartanyants, J. Synchrotron Rad. **22**, 1345 (2015).
- [24] T. Senkbeil, T. Mohamed, R. Simon, D. Batchelor, A. Di Fino, N. Aldred, A. S. Clare, and A. Rosenhahn, Anal. Bioanal. Chem. **408**, 1487 (2016).
- [25] O. Y. Gorobtsov, U. Lorenz, N. M. Kabachnik, and I. A. Vartanyants, Phys. Rev. E **91**, 062712 (2015).
- [26] K. Stachnik, I. Mohacsi, I. Vartiainen, N. Stuebe, J. Meyer, M. Warmer, C. David, and A. Meents, Appl. Phys. Lett. **107**, 011105 (2015).

References

- [27] M. Krenkel, M. Töpperwien, C. Dullin, F. Alves, and T. Salditt, *AIP Advances* **6**, 035007 (2016).
- [28] A. Ruhlandt, M. Krenkel, M. Bartels, and T. Salditt, *Phys. Rev. A* **89**, 033847 (2014).
- [29] C. Y. J. Hémonnot, J. Reinhardt, O. Saldanha, J. Patommel, R. Graceffa, B. Weinhausen, M. Burghammer, C. G. Schroer, and S. Köster, *ACS Nano* (2016), doi: 10.1021/acsnano.5b07871.
- [30] A. Chiovitti, P. Heraud, T. M. Dugdale, O. M. Hodson, R. C. A. Curtain, R. R. Dagastine, B. R. Wood, and R. Wetherbee, *Soft Matter* **4**, 811 (2008).
- [31] R. Holland, T. M. Dugdale, R. Wetherbee, A. B. Brennan, J. A. Finlay, J. A. Callow, and M. E. Callow, *Biofouling* **20**, 323 (2004).
- [32] A. M. Smith and J. A. Callow, *Biological Adhesives* (Springer, Berlin, 2006).
- [33] A. R. von Gundlach, V. M. Garamus, T. Gorniak, H. A. Davies, M. Reischl, R. Mikut, K. Hilpert, and A. Rosenhahn, *Biochimica et Biophysica Acta (BBA) - Biomembranes* **1858**, 918 (2016).
- [34] Q. Chai, B. Singh, K. Peisker, N. Metzendorf, X. Ge, S. Dasgupta, and S. Sanyal, *J Biol. Chem.* **289**, 11342 (2014).
- [35] S. Baier, C. D. Damsgaard, M. Scholz, F. Benzi, A. Rochet, R. Hoppe, T. Scherer, J. Shi, A. Wittstock, B. Weinhausen, J. B. Wagner, C. G. Schroer, and J.-D. Grunwaldt, *Microscopy and Microanalysis* **22**, 178 (2016).
- [36] A. Wittstock, V. Zielasek, J. Biener, C. M. Friend, and M. Bäumer, *Science* **327**, 319 (2010).
- [37] S. Baier, A. Wittstock, C. D. Damsgaard, A. Diaz, J. Reinhardt, F. Benzi, J. Shi, T. Scherer, D. Wang, C. Kübel, C. G. Schroer, and J.-D. Grunwaldt, *Nanoscale* (2016), submitted.
- [38] W. Ding, M. Klumpp, S. Lee, S. Reuß, S. A. Al-Thabaiti, P. Pfeifer, W. Schwieger, and R. Dittmeyer, *Chemie Ing. Tech.* **87**, 702 (2015).
- [39] C. Holse, C. F. Elkjær, A. Nierhoff, J. Sehested, I. Chorkendorff, S. Helveg, and J. H. Nielsen, *J. Phys. Chem. C* **5**, (119).
- [40] D. E. Doronkin, S. Baier, T. Sheppard, F. Benzi, and J.-D. Grunwaldt, *J. Phys. Conf. Ser.* (2016), accepted for publication.
- [41] G. Hofmann, A. Rochet, S. Baier, M. Casapu, S. Ritter, F. Wilde, M. Ogurreck, F. Beckmann, and J.-D. Grunwaldt, *J. Phys. Conf. Ser.* **499**, 012017 (2014).

- [42] R. Hoppe, J. Reinhardt, G. Hofmann, J. Patommel, J.-D. Grunwaldt, C. D. Damsgaard, G. Wellenreuther, G. Falkenberg, and C. G. Schroer, *Appl. Phys. Lett.* **102**, 203104 (2013).
- [43] J.-D. Grunwaldt and C. G. Schroer, *Chem. Soc. Rev.* **39**, 4741 (2010).
- [44] J. Wagner and J. M. Köhler, *Nano Lett.* **5**, 685 (2005).
- [45] M. Rahman and E. Rebrov, *Processes* **2**, 466 (2014).
- [46] M. Luty-Błocho, K. Fitzner, V. Hessel, P. Löb, M. Maskos, D. Metzke, K. Paclawski, and M. Wojnicki, *Chem. Eng. J.* **171**, 279 (2011).
- [47] G. Hofmann, G. Tofighi, G. Rinke, S. Baier, A. Ewinger, A. Urlab, A. Wenka, S. Heideker, A. Jahn, R. Dittmeyer, and J.-D. Grunwaldt, *J. Phys. Conf. Ser.* (2016), accepted for publication.
- [48] M. Beckers, T. Senkbeil, T. Gorniak, M. Reese, K. Giewekemeyer, S.-C. Gleber, T. Salditt, and A. Rosenhahn, *Phys. Rev. Lett.* **107**, 208101 (2011).
- [49] J. Rothe, J.-D. Grunwaldt, and S. Doyle, *Synchr. Rad. News* **29**, 9 (2016).